VIP **Very Important Paper**

Special Issue

Electrodeposition of Silver Vanadate Films: A Tale of Two Polymorphs

Abbas Vali,[a] Hori P. Sarker,[b] Hyung-Woo Jee,[c] Attila Kormányos,[d, e] Farinaz Firouzan,[a] Noseung Myung,[f] Ki-Jung Paeng,[c] Muhammad N. Huda,[b] Csaba Janáky,[d, e] and Krishnan Rajeshwar*[a]

Two polymorphs of $AgVO_3$, namely the α- and β- forms, were prepared and their physical, structural, optical, electrochemical, and photoelectrochemical characteristics were compared using a battery of experimental and theoretical tools. A two-step method, previously developed in the our laboratory for the electrodeposition of inorganic semiconductor films, was applied to the electrosynthesis of silver vanadate ($AgVO_3$) films on transparent, conducting oxide surfaces. In the first step, silver was cathodically deposited from a non-aqueous bath containing silver nitrate. In the second step, the silver film was anodically stripped in an aqueous medium containing ammonium metavanadate. The anodically generated silver ions at the interface underwent a precipitation reaction with the vanadate species to generate the desired product in situ. Each of these steps were mechanistically corroborated via the use of electrochemical quartz crystal microgravimetry, used in conjunction with voltammetry and coulometry. As-deposited films were crystalline and showed p-type semiconductor behavior. Theoretical insights are provided for the electronic origin of the α→β phase transformation in $AgVO_3$ and the disparate optical band gaps of the two polymorphs. Finally, implications for the application of this material in solar cells are provided.

1. Introduction

Silver oxide based semiconductors have recently come under the spotlight in the continued search for candidates for photovoltaic solar cells, solar water splitting, CO_2 photoreduction, and environmental remediation applications.[1] Of these, ternary compounds generated from the two binary components, namely, Ag_2O and V_2O_5, and exhibiting a range of $Ag_2O:V_2O_5$ stoichiometries (1:7, 1:2, 1:1, 2:1, 3:1; see Figure 1), have elicited both fundamental and practical interest (see

review in Ref. 2). In particular, $AgVO_3$ has attracted considerable interest because of its wide-ranging practical applications including batteries, sensors, antibacterial formulations, and as photocatalysts for pollutant decomposition.[3–16]

Polymorphism in $AgVO_3$ has provided a platform for many studies; this compound exhibits up to four different crystallographic forms, namely, α, β, γ and δ forms.[2] The most common are the metastable α and thermodynamically- stable β polymorphs with monoclinic space groups *Cm* and *C2/c*, respectively.[2,15] The structural aspects of the two polymorphs and the component AgO_x and VO_4 clusters in them along with their relative juxtapositions, are well described in the literature.[3,4,13,14,16] It is worth noting, that aside from an early study,[3] we are not aware of too many other instances where the two polymorphs have been directly compared. Hydrothermally-derived α-$AgVO_3$ microrods were transformed to β-$AgVO_3$ nanowires; the battery performance of the latter was observed to be superior in galvanostatic discharge-charge measurements.[4] Examining another study on microwave-assisted hydrothermal synthesis,[7] the photocatalytic activity of β-$AgVO_3$ appears to be superior to α-$AgVO_3$ although this comparison is confounded by the higher surface area of the β-polymorph.

As reviewed by other authors,[2] this ternary compound has been synthesized in a range of nanostructures (nanorods, nanobelts, nanoribbons, and nanowires) using methods ranging from hydrothermal (most common) to biomineralization along with other hybrid and more esoteric approaches including the use of pulsed laser deposition, microwave assistance, ultrasonic agitation etc. Conspicuous in its absence is the use of electrodeposition[17–23] for $AgVO_3$ synthesis. Given the versatility of electrosynthetic procedures,[17–23] this omission is rather surprising. This paper therefore describes the application of the

[a] A. Vali, F. Firouzan, Prof. K. Rajeshwar
Department of Chemistry and Biochemistry
The University of Texas at Arlington
Arlington, Texas 76019 (USA)
E-mail: rajeshwar@uta.edu

[b] H. P. Sarker, Prof. M. N. Huda
Department of Physics
The University of Texas at Arlington
Arlington, Texas 76019 (USA)

[c] H.-W. Jee, Prof. K.-J. Paeng
Department of Chemistry
Yonsei University
Wonju, Kangwon, 26493 (Korea)

[d] A. Kormányos, Prof. C. Janáky
Department of Physical Chemistry and Materials Science
University of Szeged
Rerrich Square 1
Szeged, H-6720 (Hungary)

[e] A. Kormányos, Prof. C. Janáky
MTA-SZTE, Lendület Photoelectrochemistry Research Group
Szeged, H-6720 (Hungary)

[f] Prof. N. Myung
Department of Energy & Materials
Konkuk University Glocal Campus
Chungju, Chungbuk 26493 (Korea)

Figure 1. Composition line diagram showing the five stoichiometries in the Ag—V—O ternary system.

First Step

$Ag^+ + e^- \rightarrow Ag$

$E^0 = +0.8$ V vs NHE

Second Step

$Ag \rightarrow Ag^+ + e^-$

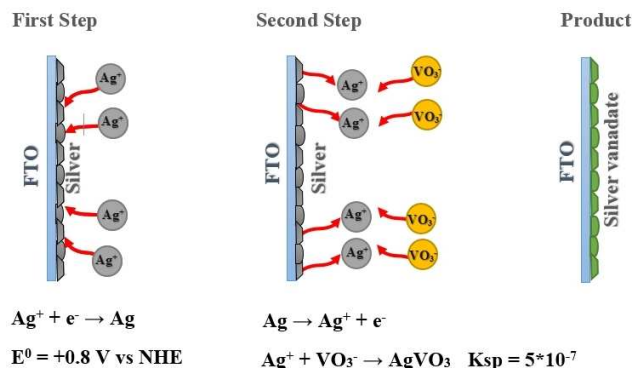$Ag^+ + VO_3^- \rightarrow AgVO_3$ $Ksp = 5*10^{-7}$

Product

Figure 2. Schematic diagram for the two-step electrosynthesis of $AgVO_3$.

two-step approach (Figure 2), previously developed in the Rajeshwar laboratory,[24–28] for the electrodeposition of $AgVO_3$ films on transparent, conducting oxide glass (fluorine-doped tin oxide or FTO) substrates.

The two-step approach was previously used for the electrosynthesis of metal chalcogenides and bismuth vanadate ($BiVO_4$).[24–28] This method hinges on the tunability afforded by the tremendous electric field strength that exists across an electrode/electrolyte interphase (nominally, several million V/cm) to tweak precursor ion fluxes. This feature, coupled with the usual variables in *homogeneous* aqueous reaction scenarios (e.g., solution pH), considerably enhances the synthetic scope as demonstrated in this study, for the $AgVO_3$ case.

In a more general sense, this study also serves to demonstrate the use of electrodeposition as a scalable preparation methodology for solar cell applications of complex metal oxides. Thus far, this methodology has been confined largely for such preparation of *binary* metal oxides or chalcogenides.[17–23] In the case of multinary chalcogenides (e.g., copper zinc tin sulfide or CZTS), a *hybrid* strategy, combining, for example, metal electrodeposition followed by sulfidation,[29] was employed unlike the strategy in this study. In the present case, both the component steps are electrochemical in origin with attendant advantages as elaborated elsewhere.[17,20,21]

2. Results and Discussion

2.1. Mechanistic Insights into the Two-Step Electrodeposition of $AgVO_3$

The choice of a non-aqueous electrolyte for silver deposition was prompted by the need to avoid hydrogen evolution and to secure metal films free from oxide contamination. To this end,

the solutions were purged with nitrogen to prevent the oxygen reduction reaction (ORR). Figure S1 compares the cyclic voltammograms for silver ion reduction and silver stripping on Pt (solid line) and FTO (dashed line) electrode surfaces. The reduction wave is shifted more negative and the leading edge of the stripping wave is more drawn out for FTO relative to Pt. These trends are reflective of the higher series resistance for FTO and the more sluggish electron transfer kinetics relative to the Pt surface. Importantly, however, the overall voltammetry profiles are otherwise essentially similar in the two cases.

The cross-over of the forward (reduction) and reverse (oxidation) voltammetry traces indicates the nucleation/growth of silver on the FTO substrate.[30,31] The sharp current drop after the anodic wave (peaking at +0.75 V for FTO) indicates the complete anodic stripping of metallic silver (Figure S1). Similar behavior could be seen for Pt, albeit at a more negative potential (~0.56 V) for the stripping wave. Based on these data, the silver film was prepared by sweeping the potential from +0.15 to −0.80 V 10 times at a 25 mV/s scan rate.

Figure S2 contains the EQCM-voltammetry-coulometry data for the first step; Figure S2a contains the frequency change and the cathodic Ag deposition voltammetry regime. The frequency decrease along the reduction wave domain is diagnostic of mass gain and the electrodeposition of a film (presumably Ag) on the Pt-coated quartz surface.[27,28,32] Further insight into the deposition mechanism can be gleaned by combining the EQCM data with coulometric assay for the reduction [Eq. (1)]:[32–34]

$$Q = - \left(\frac{nFk}{M}\right) \Delta f \tag{1}$$

Q is the charge consumed, F is the Faraday constant, Δf is the frequency change, k is the Sauerbrey constant,[32–34] and M is the molar mass of the deposit. By constructing a Q versus $-\Delta f$ plot (Figure S2b), one can calculate the electron stoichiometry, n from the slope. The calculated n value from the least-squares fitted slope was 0.94, sensibly close to the value expected from the following reduction process [Eq. (2)]:

$$Ag^+ + e^- \rightarrow Ag \tag{2}$$

The XRD and EDS patterns of the as-synthesized silver film are shown in Figures S3 and S4, respectively. These results, along with the EQCM-voltammetry-coulometry data, unequivocally confirm that the synthesized film is composed of pure elemental silver. In the second step, the silver film was stripped anodically to generate Ag^+ in an aqueous solution of ammonium metavanadate (pH: 7.0). Subsequent in situ precipitation of these ions with VO_3^-, driven by the low solubility
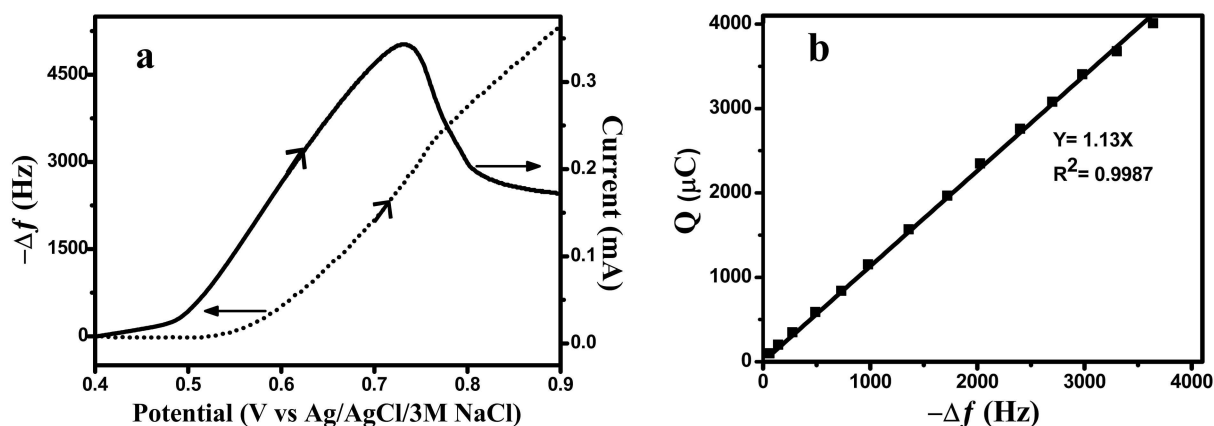
Figure 3. (a) Linear sweep voltammogram (—) and the corresponding EQCM frequency change (….) for the electrodeposition of silver vanadate at 15 mV/s potential scan rate. (b) Charge–frequency change plot derived from the EQCM-voltammetry data.

product for $AgVO_3$ ($K_{sp} = 5.0 \times 10^{-7}$)[35] yielded a *green* $AgVO_3$ film on the substrate. The choice of the above medium pH for the anodic stripping stage reflects literature evidence[36] for the preponderance of VO_3^- species in the 6.0–9.0 range. At higher pH values, other species (VO_4^{3-}) become more stable.

A linear sweep voltammogram (solid line) and the corresponding EQCM frequency change (dotted line) during film deposition, are shown in Figure 3a. The frequency decrease during the positive-going scan is diagnostic of mass gain according to the following scheme [Eqs. (3),(4)]:

$$Ag \rightarrow Ag^+ + e \qquad (3)$$

$$Ag^+ + VO_3^- \rightarrow AgVO_3 \qquad (4)$$
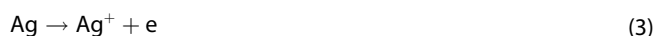
The slight lag in the mass gain relative to the current flow onset in Figure 3a is worthy of note and signals the fact that precipitation intrinsically is a kinetically slow process. The associated charge (Q) versus frequency changing ($-\Delta f$) plot of electrodeposition of $AgVO_3$ is shown in Figure 3b. The calculated n value from the slope of the least-squares fitted line was 1.06, close to the stoichiometry value expected from reaction 3.

The effect of scan rate on the potentiodynamic film growth in the second step deserves comment. A high scan rate (e.g., 25 mV/s) results in uneven film growth on the support surface. On the other hand, a low scan rate (e.g., 5 mV/s) is non-optimal from a synthesis time perspective, and importantly, also results in partial desorption of precipitated $AgVO_3$ from the support electrode surface. A potential scan rate in the range, 10–15 mV/s, was found to provide a reasonable compromise and yielded good film adhesion and product quality (see below).

2.2. Physical Characterization of the Silver Vanadate Film

Interestingly, XRD pattern of the as-prepared film (Figure S5) showed that the synthesized film was crystalline (even without

thermal anneal) in α-$AgVO_3$ form. Significantly, this crystallinity was afforded despite the electrodeposition being conducted at ambient temperature. The as-prepared α-$AgVO_3$ film was annealed at two different temperatures, 150 °C and 250 °C, for 30 min to prepare β-$AgVO_3$. The XRD patterns of these samples (Figures S5, patterns d and e) showed that the samples annealed at 150 °C and 250 °C were in the α-$AgVO_3$ and β-$AgVO_3$ polymorphic forms, respectively. Thus, the green α-$AgVO_3$ polymorph thin film was transformed to a reddish β-$AgVO_3$ between 150 °C to 250 °C. This is in good agreement with the reported exothermic phase transformation temperature (249 °C) from α-$AgVO_3$ to β-$AgVO_3$.[37] The transformation from α-phase to β-phase was accompanied by the formation of traces of silver (the peak at 38.3° in Figure S5, pattern e). This observation is consistent with the thermolysis of β-$AgVO_3$ to Ag_2O and $Ag_2V_4O_{11,}$[38] and subsequently to Ag.[39] The presence of metallic silver in β-$AgVO_3$ was observed by TEM in previous studies.[6] Silver is of interest because of its plasmonic possibilities for solar cell applications.

Morphological examination of the *as-prepared* samples by SEM and EDS revealed excellent crystallinity and one-dimensional film growth in the form of nanorods, see Figure 4 as an example. Elemental EDS maps (not shown) indicated uniform film deposition across the entire support electrode surface. Specifically, no regions rich in silver could be found, for example. Compositional EDS assays averaged from different spots (see Experimental Section) were consistent with the film composition: $Ag_{0.94 \pm 0.02}V_{1.02 \pm 0.01}O_{2.90 \pm 0.07}$; a representative EDS trace is shown in Figure S6 in the Supplemental Information.

X-ray photoelectron spectra in the survey mode (not shown) showed no elements other than the expected Ag, V, and O along with the ubiquitous signal from (adventitious) carbon. High resolution spectra for the Ag 3d, V 2p, and O is binding energy regimes for the electrodeposited samples (not shown) were in broad agreement with those reported in the literature for samples derived from other synthesis methods.[12,13,40] Film compositional purity is critical for solar cell applications and
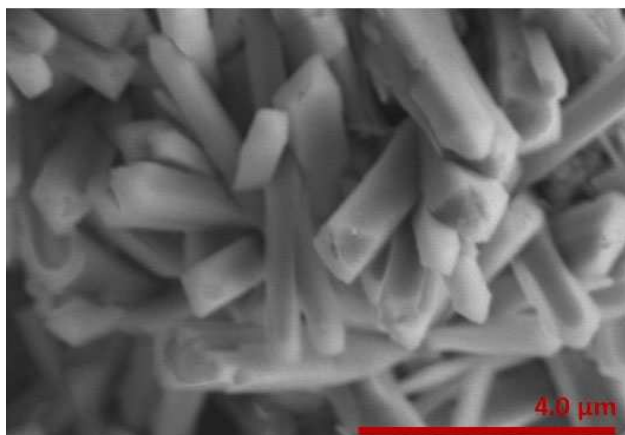
Figure 4. Representative scanning electron micrograph of an as-prepared silver vanadate film on FTO.

Table 1. Experimental and calculated energy bandgap values along with literature data.

Oxide	E_{VB} [eV][a]	Theoretical band gap [eV]		Experimental band gap [eV][b]		Literature values [eV]	Ref.
		direct	indirect	direct	indirect		
α-AgVO$_3$	−5.62	2.42	2.33[c]	2.72	2.45	2.50	3
						2.50	7
						2.22	43
β-AgVO$_3$	−5.38	2.00	1.94[d]	2.47	2.12	2.01	5
						2.04	14
						2.43	40
						~2.2	12
						2.3	7

[a] See Figure 10a below; [b] See Figures S7 and 5; [c] See Figure 7 below; [d] See Figure 8 below.

these data demonstrate that electrodeposition does meet this requirement.

2.3. Optical Properties

Tauc plots[41] were constructed from the UV/visible diffuse reflectance spectral data. Figure S7 and Figure 5 contain these plots for the as-deposited α-AgVO$_3$ samples and the β-AgVO$_3$ counterparts obtained after thermal anneal, respectively. Both direct and indirect optical transitions are indicated with corresponding energy band gaps of 2.72 eV and 2.45 eV for α-AgVO$_3$ and 2.47 eV and 2.12 eV for β-AgVO$_3$, respectively. Table 1 presents a comparison of these values with those reported in the literature for samples prepared using other techniques. There is some scatter in the reported experimental values for the energy band gaps of the two polymorphs, and the values quoted also have varying precision (Table 1). This issue has been discussed by us elsewhere[42] and is a problem associated with many confounding factors, some of which have to do with the method of extraction of the band gap values
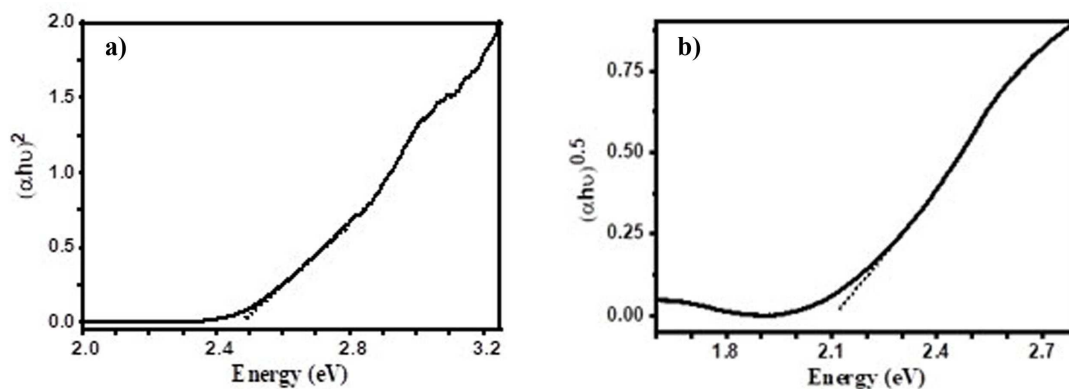
from the spectral information.[41] Nonetheless, a safe conclusion can be made that the β- polymorph has a narrower gap than the α- counterpart. The underlying factors in this trend are discussed in the next section on electronic band structure calculations.

2.4. Electronic Band Structure Calculations

The α and β-AgVO$_3$ polymorphs differ each other by their local coordination environment (c.f. Figures 6a and b). α-AgVO$_3$ has alternate layers of Ag and V polyhedral as seen from the [010] direction. In the bulk, the Ag atoms are octahedrally coordinated with 6 O atoms while the V atoms are tetrahedrally coordinated with 4 O atoms. There are two types of AgVO$_6$ octahedra differing in the Ag—O bond lengths. The first type of Ag(1) atoms has 3 pairs of Ag(1)—O distinct bond lengths (2.45 Å, 2.50 Å and 2.55 Å) and the second type of Ag(2) atoms has another 3 pairs of Ag(2)—O distinctly different bond lengths (2.38 Å, 2.42 Å and 2.53 Å). Within a chosen Ag layer, Ag octahedra share their edges to form the Ag layer and two adjacent Ag layers are connected via the VO$_4$ layer by making —O—Ag (1st layer)-O—V—O—Ag (2nd layer)-O— extended chains.

Figure 5. Tauc plots for β-AgVO$_3$ film on FTO. Frames (a) and (b) contain the plots analyzed for direct and indirect optical transitions, respectively.
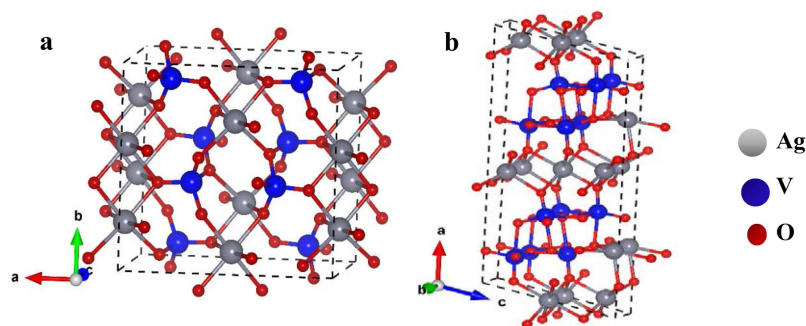
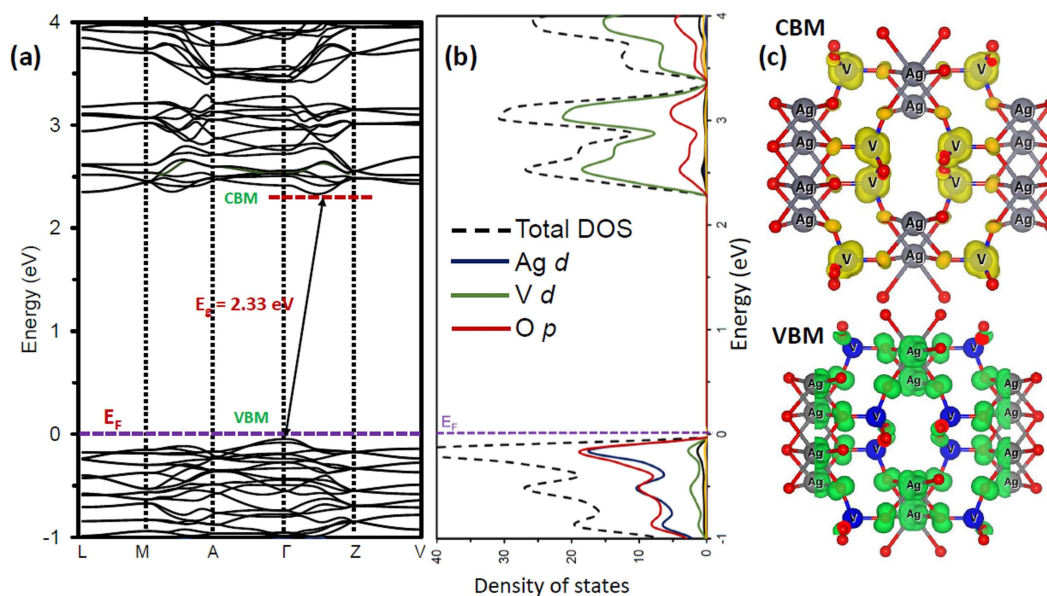**Figure 6.** DFT + U relaxed unit cells for a) α-AgVO₃ and b) β-AgVO₃.

Figure 7. a) Band structure and b) partial density of states of α-AgVO₃ and c) Band decomposed charge density of valence band maxima (VBM; bottom panel) and conduction band minima (CBM; upper panel) for α-AgVO₃.

Thus, the V-containing layers get interlocked between two adjacent Ag layers. Note, that within the α-phase, there is only one type of VO₄ polyhedron having three distinct V–O bond lengths (1.80 Å in one pair, 1.66 Å and 1.64 Å) and within a given V layer there is an extended chain of –O–V–O–V–O– bonds.

Unlike in α-AgVO₃, the layered structure transforms into stepwise broken polyhedron layer in β-AgVO₃ (Figure 6b). In contrast with one type of AgVO₆ polyhedron in the α-phase, the Ag atom is coordinated with O atoms in three different ways: AgVO₇, AgVO₆ and AgVO₅ in β-AgVO₃. The Ag–O bond lengths vary from 2.35 Å to 2.90 Å. On the other hand, V atom is coordinated with 5 O atoms as in a VO₅ cluster (unlike the VO₄ unit in the α-phase) and the V–O bond lengths range from 1.60 Å to 2.15 Å. Thus, the Ag and V polyhedra in the β-phase are more distorted in terms of coordination as well as bond lengths compared to the α-phase. Due to the transformation from α to β-phase (see below), the Ag layer and V layers are formed in zigzag fashion. In a given layer, both Ag–O and V–O bonds are present in the β-phase whereas in α-phase, this type

of bonding pattern is absent. In β-phase, –O–V–O–V–Ag–O–Ag–O–Ag–O– connectivity is present. Thus α-phase transforms to the more stable β-phase via distortion by breaking the layered structure as well as changing the coordination of Ag and V atoms.

The lattice parameters and the atomic positions in the crystal structures of the two polymorphs were optimized prior to the band structure calculations. Figures 6a and b depict the unit cells containing 8 Ag atoms, 8 V atoms and 24 O atoms within the unit cell for both polymorphs. The calculated and experimental lattice parameter values along with other reported results[15,37,38] are presented in Table S1. The calculated values are in good agreement with the experimental values for both polymorphs of AgVO₃ except for the β angle in α-AgVO₃. The calculated β angle of α-AgVO₃ is overestimated compared to the experimental value by 11.0% but it is close to the reported theoretical results in a previous study.[15]

Figures 7a and b show the DFT + U-derived electronic band structure and partial density of states (pDOS) for α-AgVO₃. The
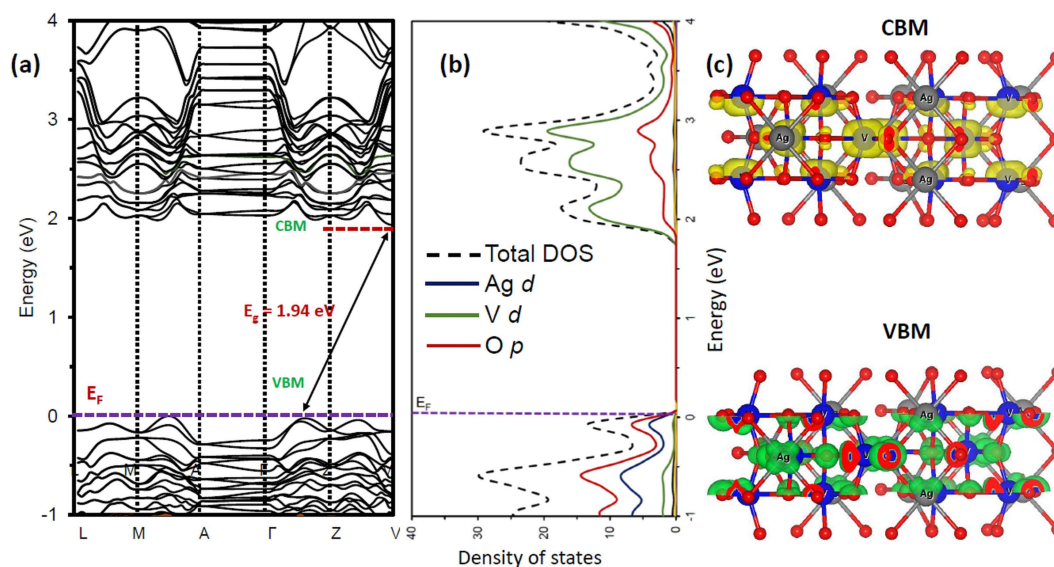
Figure 8. a) Band structure and b) partial density of states (pDOS) of β-AgVO$_3$ and c) Band decomposed charge density of valence band maxima (VBM; bottom panel) and conduction band minima (CBM; top panel) for β-AgVO$_3$.

Fermi energy level is defined as the highest occupied electronic state and is indicated by 0 eV. The valence band is mainly composed of Ag 4d and O 2p states, as seen in the partial density of states plot (Figure 7b) and in the band decomposed charge density plot (Figure 7c, bottom panel). The Ag 4d and O 2p states are strongly hybridized in the valence band. The dispersion of valence band along all the high symmetry directions in the Brillouin zone indicates that the photoexcited holes have low effective mass.

The conduction band of α-AgVO$_3$ is mainly composed of anti-bonding V 3d and O 2p states, as seen in the partial density of states plot (Figure 7b, right panel) and the band decomposed charge density plot of (Figure 7c, top panel). The strongly hybridized bonding part of V 3d and O 2p appears at the bottom of the valence band, as can be seen in Figure 7b. The total width of the valence band is 4.5 eV, which is bounded by strongly hybridized Ag d and V d bands from the upper and at the bottom side, respectively. The fundamental band gap of α-AgVO$_3$ is indirect in nature, because the conduction band minima (CBM) is located between the Γ and Z points and the valence band maxima (VBM) is placed at point Γ. The calculated indirect bandgap is 2.33 eV which is close to the band gap value (2.45 eV) obtained via DRS and the calculated direct gap is 2.42 eV (Table 1). The calculated electronic band structure and density of states plot have similar features with another reported result,[15] but the calculated indirect band gap by the B3LYP and HSE06 methods overestimate the reported experimental band gap value by 52% and 38%, respectively. On the other hand, the PBE calculation underestimates the reported experimental indirect band gap by 28%.

Figures 8a and b show the electronic band structure and partial density of states (pDOS) for β-AgVO$_3$. From the density of states plot and band-decomposed charge density plot of VBM (in Figures 8b and c (bottom panel), respectively) we see

that, here again, the valence band is mainly composed of Ag 4d and O 2p states. However, for β-AgVO$_3$, Ag 4d and O 2p are not as strongly hybridized near the Fermi level as they are for α-AgVO$_3$. The calculated pDOS (Figure 8b) and band-decomposed charge density of CBM plot (Figure 8c, upper panel) confirm that the conduction band of β-AgVO$_3$ is composed of V 3d and O 2p states with predominent contribution of V 3d orbitals. Note that near the CBM of β-AgVO$_3$, the contribution from V 3d is not as prominent as in α-AgVO$_3$. Similarly, at the bottom of the valence band, the bonding part of V 3d and O 2p hybridization is not as strong as in α-AgVO$_3$.

The valence band witdh is about 5.5 eV, which is 1 eV wider than in that of α-AgVO$_3$. This implies that electron correlation strength in α-phase is higher than in the β-AgVO$_3$ phase. The theoretical fundamental bandgap of β-AgVO$_3$ is indirect in nature because the CBM is located at point V and VBM is located between the Γ and Z points. The calculated indirect gap of β-AgVO$_3$ is 1.94 eV which is close to the redundant indirect band gap (2.12 eV) obtained via DRS and the calculated direct gap is 2.00 eV (Table 1). The calculated electronic band structure and density of states in this study have broad similarity with the other reported results in the literature.[12,15]

The fact that β-AgVO$_3$ has a smaller band gap compared to the α-phase, can be explained as stemming from the electronic structure calculations. As described above, in the α-phase, the V 3d–O 2p bonding orbitals at the lower part of the valence band are strongly hybridized than in the β-phase. Namely, at the lower part of the valence band in the α-phase, from −3.5 eV to −4.5 eV, there is a significant contribution from V 3d orbitals (mainly from d$_{z^2}$ and d$_{x^2-y^2}$); in fact, of the two cations, the V d-band has the highest peak in the valence band. This strong bonding (V 3d–O 2p) in the α-phase also pushes anti-bonding bands in the CBM to higher energy. The overall presence of this highly-localized, occupied 3d band is responsible for the
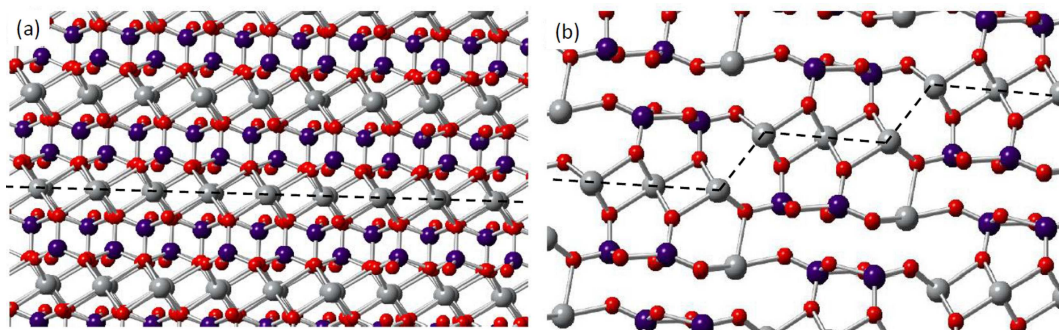
Figure 9. (a) α-AgVO$_3$ and (b) β-AgVO$_3$ crystal structures to compare the structural relaxation during the α-to-β phase transformation. The α→β transition is exothermic. The dashed line in frame (a) shows the 1D linear chain in α-AgVO$_3$. Along the y-direction, the layers are 6.919 Å apart. Gray, red and purple balls represent Ag, O and V atoms, respectively.

relatively narrow width of α-phase's valence band, compared to that of the β-phase.

In β-AgVO$_3$, the presence of V 3d is much reduced, and relatively delocalized Ag 4d band becomes more prominent. Hence, not only the valence band of β-AgVO$_3$ becomes wider, the VBM of the β-phase becomes a little higher due to the relative energetics of the atomic 3d and 4d orbitals. From a structural point of view, the α-phase contains V—O tetrahedra (even though asymmetric), a signature feature of d-orbital bonding, and are 'locked' in between the Ag—O layers (see Figure 9 below). These 'locked' V—O tetrahedra structures are responsible for the presence of the highly localized 3d electrons in the valence band. On the other hand, in the β-phase, V—O tetrahedra are distorted enough to stabilize to near V^{5+} oxidation state, which is a preferable 3d^0 state resulting in a wider valence band.

2.5. Electronic Origin of the α-to-β Phase Transformation in AgVO$_3$

From the electronic structures discussed above, we now re-iterate several observations: (i) Anti-bonding O 2p and Ag 4d hybridization near the top of the valence band is stronger in the α-phase than in β-phase, whereas the bonding hybridizations are at about −17 eV below the Fermi level (not shown in the figure) for both the phases. (ii) Similarly, O 2p and V 3d hybridization at the bottom of valence band is stronger in the α-phase than in β-phase. (iii) The valence band width in the α-phase is 1 eV narrower than that of the β-phase. These all imply that electron correlation is stronger in the α-AgVO$_3$ polymorph. Note that, strongly hybridized V 3d with O 2p band in α-AgVO$_3$ at the bottom of the valence band implies some electronic occupation of V 3d band. Hence, the oxidation state of V in α-AgVO$_3$ is not exactly +5, rather V$^{+(5-\delta)}$. Figure 9a shows very symmetric V—O tetragonal bonding features in α-AgVO$_3$.

As seen in Figure 9a, the strongly hybridized O 2p and Ag 4d anti-bonding features create layers of Ag—O polyhedra in α-AgVO$_3$. These polyhedra line-up as a linear structure within the crystal along the z-direction, separated by about 7 Å in the y-

direction. The nearest Ag—Ag distance is along the z-direction, 3.326 Å, which is shown in the figure. The other structural nuances in the two polymorphs were noted earlier.

Apart from the fact that the α to β phase transformation requires electron-phonon interaction energy, two other points to be noted. Firstly, the 1-D periodic arrangement of Ag atoms in α-AgVO$_3$ transforms into irregular doublet units with a longer periodic range in β-AgVO$_3$ (compare the two frames in Figure 9), and the d orbitals in this phase become more stabilized. The stabilization of Ag 4d band in β-AgVO$_3$ can be verified by observing the shift of the Ag-d pDOS peaks at the VBM, compare Figure 7b with Figure 8b. This type of stabilization of the overall structure due to distortion of the 1-D geometry is a signature of Peierls-type of distortion. However, we note that Peierls distortion as defined, strictly requires a partially filled band, whereas the Ag d band here is fully occupied.

Secondly, a given horizontal layer in β-AgVO$_3$ has both V—O and Ag—O bonds, whereas before the α to β phase transformation, the V—O layers did not contain any Ag atoms. This results in some vertical V—O bonds breaking in β-AgVO$_3$ as should be evident from Figure 9b. This second event enables V atoms to jettison some 3d electrons, and hence, reach a (more favorable) V^{+5} oxidation state. These two phenomena in unison help lower the energy barrier for the α- to β-AgVO$_3$ phase transformation, and the β-AgVO$_3$ phase becomes energetically more favorable.

2.6. Conduction and Valence Band Locations in α- and β-AgVO$_3$

Ambient-pressure UV photoelectron spectroscopy (AP-UPS) was used to map the valence band maxima (VBM) in α-AgVO$_3$ and β-AgVO$_3$. Figure 10a contain the data; from the intercepts of the plots, the VBM were located. These values on the vacuum energy scale are given in Table 1 above. Using these values and the energy band gaps for the two polymorphs, the conduction and valence band positions for the two compounds can be estimated. These are given in Figure 10b. The valence band offset is 0.24 eV and these two phases have Type-I bandgap
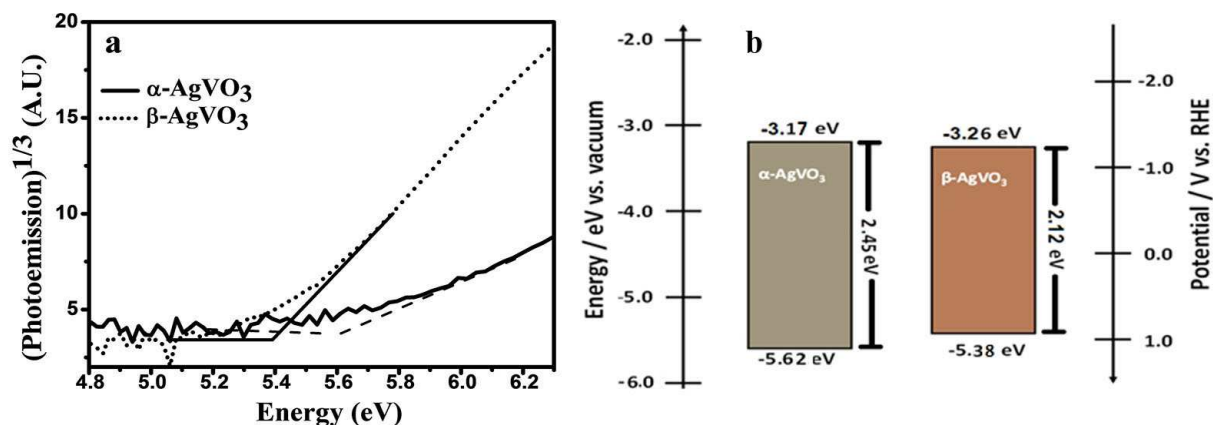
Figure 10. a) Ambient-pressure UV photoelectron spectroscopy (AP-UPS) data-derived plots for α-AgVO$_3$ and β-AgVO$_3$ and b) surface energy band positions for the two polymorphs constructed from the AP-UPS and DRS data.

offset. The theoretically-obtained valence band offset (0.19 eV), which was calculated by taking highly localized O-s band as the reference bands, agrees reasonably well with the measured value above. Clearly, the band positions are not favorable for water photooxidation. Such a conclusion is entirely consistent with the experimental findings from an earlier study[3] which noted that both α-AgVO$_3$ and β-AgVO$_3$ had zero activity for photo generating O$_2$ from water.

2.7. Electrochemical and Photoelectrochemical Behavior of α- and β-AgVO$_3$

Surface states are often exceedingly important in mediating charge transfer at the semiconductor-electrolyte interface.[44] The surface density of states (SDOS) can be accessed via the use of AP-UPS; these data for the two polymorphs (Figure 11) indicate that β-AgVO$_3$ has a higher SDOS relative to the α-polymorph. To explore the implications of this trend on the electrochemical charge transfer kinetics for the two samples,
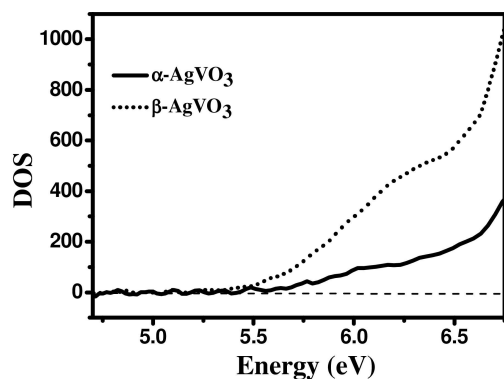
polarization experiments were conducted using a quasi-reversible redox couple, Fe(CN)$_6^{3-/4-}$. Figure 12 contains the data; for comparison, Pt and FTO electrodes were also included for these experiments. The insert in Figure 12 shows the data in Tafel plot (log i vs. E) format.[45]

The SDOS is a crucial factor in dictating the kinetics of charge transfer, both for metal and semiconductor electrodes.[45] In general, the SDOS follows the trend: metal > degenerately-doped semiconductor > nominally-doped semiconductor. Consistent with this, the charge transfer kinetics, inferred from Figure 12 for the oxidation of Fe(CN)$_6^{4-}$ redox species are ordered thus: Pt > FTO > β-AgVO$_3$ > α-AgVO$_3$. Further, the trend for the two polymorphs is entirely in accordance with the SDOS data in Figure 11. It is worth noting in the experiments in Figure 12 that anodic polarization translates to the forward-bias
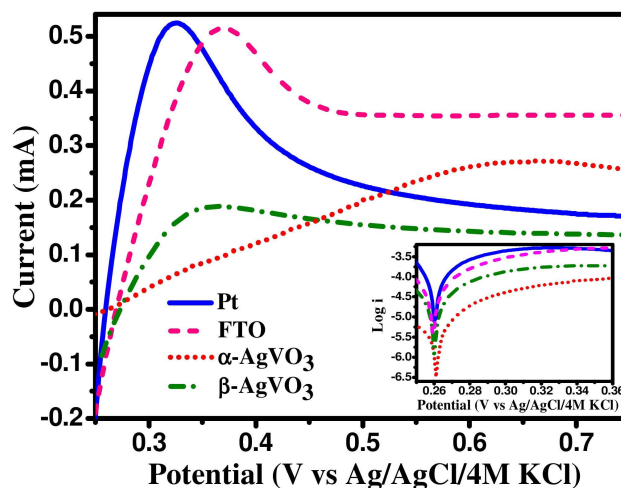

Figure 11. Ambient-pressure UV photoelectron spectroscopy (APUPS) data-derived plots for α-AgVO$_3$ and β-AgVO$_3$.

Figure 12. Forward-bias current–potential polarization curves in the dark for the oxidation of Fe(CN)$_6^{4-}$ redox species in 0.5 M KNO$_3$ supporting electrolyte at a potential scan rate of 5 mV/s. The insert contains these data in Tafel plot format. The standard redox potential, E^0, for the couple: Fe(CN)$_6^{3-}$ + e$^-$ → Fe(CN)$_6^{4-}$ is + 0.361 V vs. NHE (+ 0.164 V vs. Ag/AgCl).
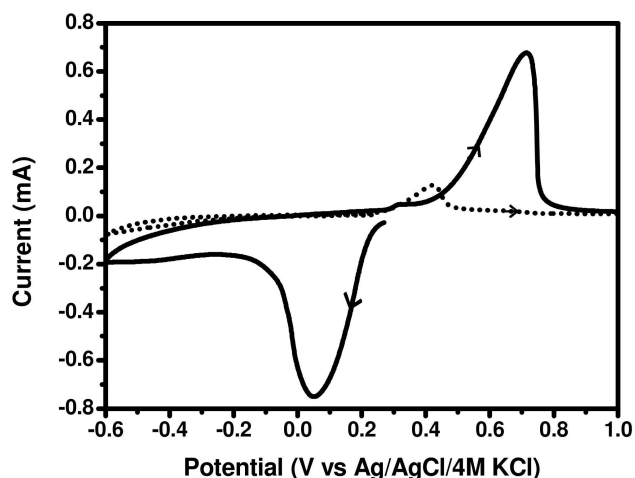
Figure 13. Cyclic voltammograms of as-prepared $AgVO_3$ film in 0.2 M sodium sulfate in water (–) and 0.2 M tetrabutylammonium perchlorate in acetonitrile (….), 5 mV/s potential scan rate.
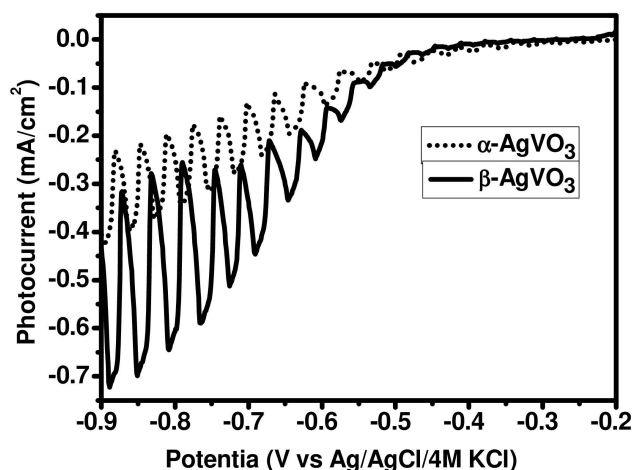

Figure 14. Linear sweep photovoltammograms for α-$AgVO_3$ (–) and β-$AgVO_3$ (….) in dioxygen-purged 0.2 M tetrabutylammonium perchlorate in acetonitrile, 1 mV/s potential scan rate.

regime for a *p*-type semiconductor such as $AgVO_3$. Note also, in this regard, that the DFT calculations presented earlier, placed the Fermi level close to the VBM in line with *p*-type conductivity behavior for the two polymorphs.

Electrochemical and photoelectrochemical stability plays a crucial role in dictating the practical applicability of a given semiconductor.[44] To probe the stability of the material in the dark, cyclic voltammetry experiments were performed. Figure 13 contains the data. In aqueous 0.2 M sodium sulfate, the as-prepared $AgVO_3$ shows a cathodic wave on scanning from the rest potential. An anodic wave is seen on the return scan. Comparison with the cyclic voltammetry data in Figure 13 immediately establishes these features to arise from the anodic generation of Ag^+ species leaching out of the film and their subsequent reduction on the return scan. On the other hand, these features are greatly attenuated in the non-aqueous medium. The faint reduction wave on the return scan in the non-aqueous case can be attributed to residual traces of water in acetonitrile. The data in Figure 13 are consistent with the anodic corrosion reaction [Eq. (5)]:

$$2AgVO_3 + H_2O + 2e^- \rightarrow 2Ag + V_2O_5 + 2OH^-$$
$$E^0 = +0.07 \text{ V vs NHE}$$

(5)
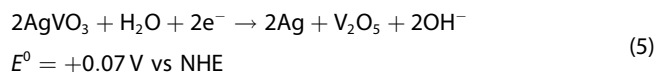
The standard potential for the above reaction was calculated from thermodynamic data in the literature on standard heats of formation.[35,46,47]

Having established that $AgVO_3$ has reasonable electrochemical stability in a non-aqueous electrolyte, photoelectrochemical experiments were conducted using dioxygen as an electron acceptor. Figure 14 contains the corresponding photovoltammetry[48] data for the two polymorphs.

In a photovoltammetry experiment, both the dark (electrochemical features) and the photocurrents are brought out in a single scan.[48] Note that the experiments are conducted in the *reverse-bias* regime unlike in the (forward-bias) experiments in

Figure 13. Thus, the photocurrents are induced by the minority carriers which are electrons for a *p*-type semiconductor.[44] Consistent with this notion, the photocurrent polarity is cathodic in the traces in Figure 14 in line with the *p*-type semiconductor behavior of $AgVO_3$ (see above). Note that there is significant dark current flow on increasing negative polarization for both the samples in Figure 14, suggesting that the semiconductor-electrolyte junctions in both the cases are "leaky". These currents are attributed to the reduction of (adventitious) dioxygen in the electrolyte.

The additional possibility that the dark currents arise from reduction of the oxide itself to silver (c.f., eq. 4) can be discounted based on the stability trends established in Figure 13. Clearly, the photoactivity of β-$AgVO_3$ is superior to that of α-$AgVO_3$; the photocurrents in the two cases are also reasonably high in the mA/cm^2 range. However, considerable improvement in the quality of the $AgVO_3$/electrolyte junctions is warranted before these candidates can be further considered for solar device applications.

3. Conclusions

In this study, motivated by the applicability of new-generation oxide semiconductors for solar cell applications, the synthesis and characterization of electrodeposited films of $AgVO_3$ in both aqueous and non-aqueous media, were described. Thermal anneal of the as-deposited α-$AgVO_3$ converted it to β-$AgVO_3$ and afforded comparison of the structural, optical, electronic, electrochemical, and photoelectrochemical attributes of the two polymorphs. From a theoretical perspective, it has been shown here, to the best of our knowledge for the first time, that the driver of the exothermic $\alpha \rightarrow \beta$ $AgVO_3$ phase transformation is the structural relaxations due to a Peierls-like distortion and the tendency of V atoms to gain the stable $+5$ oxidation state. Taken in whole, it is intriguing that a ternary oxide in two

polymorphic forms that only differ in the relative juxtaposition of component AgO_x and VO_4 clusters,[16] can display such diversity in optical, electronic, electrochemical, and photo-electrochemical properties. This aspect, of potential relevance to solar photovoltaic applications, deserves further scrutiny beyond the scope of the present study.

Experimental Section

Materials

Silver nitrate [$AgNO_3$ (Alfa Aesar)] and ammonium vanadate [NH_4VO_3 (Alfa Aesar)] were used as Ag and V source, respectively. Acetonitrile [CH_3CN (Sigma-Aldrich)] and double-distilled water (H_2O) were used as solvent. Tetrabutylammonium perchlorate [$CH_3CH_2CH_3CH_2)_4N(ClO)_4$ (Alfa Aesar)] and potassium nitrate [KNO_3 (Alfa Aesar)] were used to prepare electrolyte solutions. Sodium dodecyl sulfate [$CH_3(CH_2)_{11}SO_4Na$ (Sigma-Aldrich)] was used as binder. Potassium ferricyanide [$K_3[Fe(CN)_6]$ (Sigma-Aldrich)] and Potassium ferrocyanide [$K_4[Fe(CN)_6]$ (Sigma-Aldrich)] were used as redox couple sources. All the chemicals were used as received without further purification.

Electrosynthesis of AgVO$_3$ Film

In the first step, a single compartment, three-electrode cell setup was used for the electrodeposition of silver thin film. An FTO substrate (Sigma-Aldrich, sheet resistance: ∼ 7 Ω/sq) with 0.785 cm^2 area served as a working electrode. A platinum foil and Ag/AgCl/4 M KCl electrode were used as the counterelectrode and quasi-reference electrode, respectively. The electrodeposition solution contained 20 mM $AgNO_3$, 0.2 mM sodium dodecyl sulfate (as a binder), and 200 mM tetrabutylammonium perchlorate (TBAP) as a supporting electrolyte in acetonitrile. Potentiodynamic film growth was used to control the thickness (nominally, 500 nm) of the silver thin film. The potential was swept 10 times from +0.15 to −0.80 V at 25 mV/s scan rate.

In the second step, the prepared silver thin film on FTO substrate served as the working electrode. A platinum foil and Ag/AgCl/4 M KCl were again used as the counterelectrode and reference electrode, respectively. The silver thin film was stripped anodically in ammonium metavanadate solution (40 mM) to generate Ag^+ and subsequent in situ precipitation with VO_3^- to yield $AgVO_3$ thin film on the substrate (Figure 2). The silver metavanadate thin film was prepared by sweeping the potential from 1.0 V to 1.20 V at 15 mV/s scan rate. The potentiodynamic sweeps were continued till no anodic current was observed from the residual oxidation of silver.

Electrochemical Quartz Crystal Microgravimetry (EQCM)

An EG&G Princeton Applied Research 263 A instrument equipped with Power Suite electrochemistry software, a Seiko EG&G model QCA 922 instrument, and an oscillator module (QCA 922-10), was used. A single compartment, three-electrode cell setup was used for electrochemical experiments at room temperature and comprised of a 9 MHz AT-cut, Pt-coated quartz crystal (geometric area, 0.2 cm^2) working electrode, a Pt wire counterelectrode, and a Ag/AgCl/3 M NaCl reference electrode.

Physical Characterization

A Siemens D-500 instrument with a Cu Kα radiation source (λ = 1.5406 Å) was used for X-ray diffraction (XRD) analysis of the prepared films. Scanning electron microscopy (SEM) and energy dispersive spectroscopy (EDS) were performed with a Hitachi S-3000 N FE scanning electron microscope. The electron beam energy was 10 kV. The EDS data were collected from different spots of the prepared films and averaged. X-ray photoelectron spectroscopy (XPS) was performed on a Kratos Ultra DLD instrument. The source was Al K$_\alpha$ radiation at 1486.6 eV with 10.0 eV pass energy and 0.10 eV resolution. The reported binding energies were referenced against the C 1s photoelectron value of 284.6 eV.

Diffuse reflectance UV-Vis spectra were collected with an Avantes AvaSpec2048 instrument. An Avasphere-50 type integrating sphere was used with $BaSO_4$ as the reference. The reflectance data were converted to absorbance values via the Kubelka-Munk function: α/$S = (1-R)^2/2R$, where α is the absorption coefficient, S is the scattering coefficient, and R is the reflectance.[41]

Ambient-pressure UV photoelectron spectra[49] were recorded on a KP Technology APS04 Kelvin-probe instrument equipped with a 2 mm diameter gold alloy-coated tip. The Fermi level (E_F) of the tip was determined by relative to a silver reference target ($E_{F, Au tip}$ = −4.61 eV). The reference target was thoroughly polished with a 30 μm diamond paper. Ambient pressure UV photoelectron spectroscopy (APUPS) was carried out using a stationary Kelvin probe tip. The sample surface was illuminated with a 4–5 mm spot size, while the UV light source was swept in the range, λ = 180–340 nm using a monochromator.

Photoelectrochemistry

A single compartment, three-electrode cell setup and a CH Instruments potentiostat (Model CHI720 C) were used for electrochemical measurements. The prepared films were supported on FTO substrate and the counterelectrode and reference electrode were the same as those described above. The electrochemical solution contained 0.2 M tetrabutylammonium perchlorate (TBAP) in acetonitrile and was purged by dioxygen (as an electron acceptor) during the photovoltammetry measurement. The potential was swept at 1 mV/s scan rate. Both the dark and illuminated periods were 15 s. A 400 W Xe lamp was used as a radiation source at a fixed distance (15 cm) from cell. The light intensity was measured by a Newport Model 70260 radiant power meter combined with a Model 70268 probe and was 300 mW/cm^2.

Computational Methodology

The calculations were performed within the framework of spin polarized density functional theory (DFT)[50,51] as implemented in the Vienna ab initio simulation package (VASP).[52,53] The Perdew-Burke-Ernzerhof (PBE)[54] generalized gradient approximation (GGA) functional was used for exchange and correlation. The projector augmented plane wave (PAW) method[55] was used to describe the interactions between the core and valence electrons. VASP-supplied standard PAW potentials of Ag, V, and O were used for geometric optimization as well as for electronic structure calculations. The electronic basis set was expanded in terms of plane wave and kinetic energy cutoff of 600 eV throughout the calculation. For K point sampling within the first Brillouin zone, the Monkhorst-Pack (MP) scheme was deployed. The 4×4×7 and 2×9×4 k-point meshes were used for α and β-$AgVO_3$, respectively for geometric optimization which gave well-converged results.

During the geometrical optimization, the atoms in the unit cell were fully relaxed until the residual forces among the constituent atoms became less than $0.01 \, \mathrm{eV\,Å^{-1}}$. The Methfessel-Paxton smearing method with a width of 0.002 eV was used for geometric optimization. The tetrahedron method with Blöchl corrections were applied for density of states (DOS) calculations. Self-interactions of d electrons were corrected by providing an onsite Coulombic potential via the Hubbard U parameter. The rotationally invariant DFT+U method[56] was used for calculations. The on-site Coulombic interaction term (U) and exchange interaction term (J) are the main determining factors to control the magnitude of the self-interaction correction within the DFT+U calculation framework.

It is very important to choose an appropriate value of U to correct the self-interaction error in DFT calculations. One way to choose the U value is to examine how it affects certain properties of interest, i.e., lattice constants, band gap, formation energy etc., and to use these results as a guideline for further parameterization. In this study, we chose lattice constants and band gap as our properties of interest and select U value accordingly. The selected effective U ($U_{eff} = U - J$) values were 4.0 eV and 3.1 eV for Ag and V d-electrons, respectively. The J value was 1.0 eV throughout the calculation. The calculated lattice constants as well as band gap using these chosen values of U have proximity with the reported experimental values (See Table S1 and Table 1). Finally, the VESTA[57] software was used to visualize and analyze the crystal structure and band-decomposed charge density.

Supporting Information

Cyclic voltammetry for silver electrodeposition/stripping on Pt and FTO; EQCM-voltammetry-coulometry data for electrodeposition of Ag; XRD and EDS data for electrodeposited Ag on FTO; XRD and EDS on as-prepared $AgVO_3$ film on FTO; unit cell parameters for $\alpha\text{-}AgVO_3$ and $\beta\text{-}AgVO_3$ obtained from DFT+U energy minimization.

Acknowledgements

Conflict of Interest

The authors declare no conflict of interest.

Keywords: electronic band structures · optical bandgap · photocatalysis · semiconductors · solar energy

[1] M. T. Galante, P. Sotelo, M. K. Hossain, A. Vali, A. Raamann, C. Longo, R. T. Macaluso, K. Rajeshwar, *ChemElectroChem.* **2019**, *6*, 87–96.

[2] A. P. de Melo Monteiro, R. D. Holtz, L. C. Fonseca, C. H. Z. Martins, M. de Souza, L. A. V. de Luna, D. L. de Sousa Maia, O. L. Alves, *Chem. Rec.* **2018**, *18*, 1–14.

[3] R. Konta, H. Kato, H. Kobayashi, A. Kudo, *Phys. Chem. Chem. Phys.* **2003**, *5*, 3061–3065.

[4] S. Zhang, W. Li, C. Li, J. Chen, *J. Phys. Chem. B.* **2006**, *110*, 24855–24863.

[5] S.-J. Bao, Q.-L. Bao, C.-M. Li, T. P. Chen, C.-Q. Sun, Z.-L. Dong, Y. Gan, J. Zhang, *Small* **2007**, *3*, 1174–1177.

[6] J.-M. Song, Y.-Z. Lin, H.-B. Yao, F.-J. Fan, X.-G. Li, S.-H. Yu, *ACS Nano* **2009**, *3*, 653–660.

[7] G.-T. Pan, M.-H. Lai, R.-C. Juang, T.-W. Chung, T. C.-K. Yang, *I & EC Res.* **2011**, *50*, 2807–2814.

[8] P. Ju, H. Fan, B. Zhang, K. Shang, T. Liu, S. Ai, D. Zhang, *Sep. Purif. Technol.* **2013**, *109*, 107–110.

[9] C. Belver, C. Adán, S. G. Rodríguez, M. F. García, *Chem. Eng. J.* **2013**, *224*, 24–31.

[10] A. Singh, D. P. Dutta, A. Ballal, A. K. Tyagi, M. H. Fulekar, *Mater. Res. Bull.* **2014**, *51*, 447–454.

[11] W. Zhao, F. Liang, Z.-M. Jin, X.-B. Shi, P.-H. Yin, X.-R. Wang, C. Sun, Z.-Q. Gao, L.-S. Liao, *J. Mater. Chem.* **2014**, *2*, 13226–13231.

[12] H. Shi, C. Zhou, C. Zhang, *Res. Chem. Intermed.* **2015**, *41*, 7725–7737.

[13] W. Zhao, Y. Guo, Y. Faiz, W.-T. Yuan, C. Sun, S.-M. Wang, Y.-H. Deng, Y. Zhuang, Y. Li, X.-M. Wang, H. He, S.-G. Yang, *Appl. Catal. B* **2015**, *163*, 288–297.

[14] R. C. de Oliveira, M. Assis, M. M. Teixera, M. D. P. da Silva, M. S. Li, J. Andres, L. Gracia, E. Longo, *J. Phys. Chem.* **2016**, *120*, 12254–12264.

[15] A. Beltran, L. Gracia, J. Andres, E. Longo, *J. Phys. Chem.* **2017**, *121*, 27624–27642.

[16] R. C. Oliveira, M. M. Teixera, J. P. C. Costa, M. Penha, E. M. Francisco, J. S. da Silva, M. S. Li, E. Longo, L. Gracia, J. Andres, *Ceram. Int.* **2018**, *44*, 5939–5944.

[17] K. Rajeshwar, *Adv. Mater.* **1992**, *4*, 23–29.

[18] T. E. Schlesinger, K. Rajeshwar, N. R. de Tacconi, in *Modern Electroplating* (Edited by M. Schlesinger), Chapter 14, pp. 383–411, Springer, New York, **2010**.

[19] K. Rajeshwar, N. R. de Tacconi, C. R. Chenthamarakshan, *Chem. Mater.* **2001**, *13*, 2765–2782.

[20] C. Janaky, K. Rajeshwar, *Prog. Polym. Sci.* **2015**, *43*, 96–135.

[21] C. Janaky, E. Kescenovity, K. Rajeshwar, *ChemElectroChem* **2016**, *3*, 181–192.

[22] D. Kang, T. W. Kim, S. R. Kubota, A. C. Cardiel, H. G. Cha, K.-S. Choi, *Chem. Rev.* **2015**, *115*, 12839–12887.

[23] G. V. Govindaraju, G. P. Wheeler, D. Lee, K.-S. Choi, *Chem. Mater.* **2017**, *29*, 355–370.

[24] N. Myung, S. Ham, B. Choi, N. R. de Tacconi, K. Rajeshwar, *J. Electroanal. Chem.* **2005**, *574*, 367–373.

[25] S. Ham, B. Choi, N. Myung, N. R. de Tacconi, C. R. Chenthamarakshan, K. Rajeshwar, Y. Son, *J. Electroanal. Chem.* **2007**, *601*, 77–82.

[26] L. H. Dall 'Antonia, N. R. de Tacconi, W. Chanmanee, H. Timmaji, N. Myung, K. Rajeshwar, *Solid-State Lett.* **2010**, *13*, D29–D32.

[27] N. Myung, S. Ham, S. Choi, Y. Chae, W.-G. Kim, Y. J. Jeon, K. J. Paeng, W. Chanmanee, N. R. de Tacconi, K. Rajeshwar, *J. Phys. Chem. C* **2011**, *115*, 7793–7800.

[28] H.-W. Jee, K.-J. Paeng, N. Myung, K. Rajeshwar, *J. Electrochem. Soc.* **2017**, *165*, D1–D5.

[29] J. Scragg, P. Dale, L. Peter, G. Zoppi, L. Forbes, *Phys. Status Solidi B* **2013**, *245*, 1772–1778.

[30] L. H. Mendoza-Huizar, J. Robles, M. Palomar-Pardave, *J. Electroanal. Chem.* **2002**, *521*, 95–106.

[31] R. Greef, R. Peat, L. M. Peter, D. Pletcher, J. Robinson, *Instrumental Methods in Electrochemistry*, Chapter 6, pp. 210–211, Ellis Horwood, Chichester, **2001**.

[32] S. Ham, S. Jeon, M. Park, S. Choi, K.-J. Paeng, N. Myung, K. Rajeshwar, *J. Electroanal. Chem.* **2010**, *638*, 195–203.

[33] M. R. Deakin, D. A. Buttry, *Anal. Chem.* **1989**, *61*, 1147 A-1154 A.

[34] D. A. Buttry in *Electroanalyitcal Chemistry* (Edited by A. J. Bard), Vol. 17, Marcel Dekker, New York, **1991**.

[35] H. T. S. Briton, R. A. Robinson, *J. Chem. Soc.* **1930**, 2328–2343.

[36] C. F. Baes, R. E. Messmer, *The Hydrolysis of Cations*, pp. 197–210, John Wiley & Sons, New York, **1976**.

[37] S. Kittaka, Y. Yata, K. Matsuno, *J. Solid State Chem.* **1999**, *142*, 360–367.

[38] P. Rozier, J.-M. Savariault, J. Galy, *J. Solid State Chem.* **1996**, *122*, 303–308.

[39] G. B. Hoflund, Z. F. Hazos, G. N. Salaita, *Phys. Rev. B*, **2000**, *62*, 11126–1133.

[40] A. Y. S. Malkhasian, *J. Alloys Compd.* **2015**, *649*, 394–399.

[41] A. B. Murphy, *Sol. Energy Mater. Sol. Cells* **2007**, *91*, 1326–1337.

[42] D. Roy, G. F. Samu, M. K. Hossain, C. Janaky, K. Rajeshwar, *Catal. Today* **2018**, *300*, 136–144.

[43] M. Sun, R. A. Senthil, J. Pan, S. Osman, A. Khan, *Catalysts* **2018**, *8*, 392.

[44] K. Rajeshwar, in *Encyclopedia of Electrochemistry* (Edited by S. Licht), Chapter 1, pp. 3–53, Wiley-VCH, Weinheim, **2001**.

[45] A. J. Bard, L. R. Faulkner, *Electrochemical Methods. Fundamentals and Applications.* 2th ed., Chapter 3, pp. 103 and 125, Second Edition, John Wiley & Sons, **2001**.

[46] *Lange's Handbook of Chemistry*, 11th ed. Chapter 9, pp. 4–128, McGraw-Hill, New York, **1978**.

[47] *CRC Handbook*, 84th ed. Chapter 3, pp. 85–86, CRC Press, Boca Ratón, Florida, **2003**.

[48] K. K. Mishra, K. Rajeshwar, *J. Electroanal. Chem.* **1989**, *273*, 169–182.

[49] I. D. Baikie, A. C. Grain, J. Sutherland, J. Law, *Appl. Surf. Sci.* **2014**, *323*, 45–53.

[50] P. Hohenberg, W. Kohn, *Phys. Rev.* **1964**, *136*, B864–871.

[51] W. Kohn, L. J. Sham, *Phys. Rev.* **1965**, *140*, A1133–1138.

[52] G. Kresse, J. Furthmüller, *Comput. Mater. Sci.* **1996**, *6*, 15–50.

[53] G. Kresse, J. Furthmüller, *Phys. Rev. B.* **1996**, *54*, 11169–11186.

[54] J. P. Perdew, K. Burke, M. Ernzerhof, *Phys. Rev. Lett.* **1996**, *77*, 3865–3868.

[55] P. E. Blöchl, *Phys. Rev. B.* **1994**, *50*, 17953–17979.

[56] S. L. Dudarev, G. A. Botton, S. Y. Savrasov, C. J. Humphreys, A. P. Sutton, *Phys. Rev.* **1998**, *B57*, 1505–1509.

[57] K. Momma, F. J. Izumi, *Appl. Crystallogr.* **2008**, *41*, 653–658.